

Optimising O-to-U Band Transmission Using Fast ISRS Gaussian Noise Numerical Integral Model

Mindaugas Jarmolovičius , Daniel Semrau, Henrique Buglia , Mykyta Shevchenko , Filipe M. Ferreira , Eric Sillekens , Polina Bayvel  and Robert I. Killey

Abstract—We model the transmission of ultrawideband (UWB) signals, including wavelength-dependent fibre parameters: dispersion, nonlinear coefficient and effective fibre core area. To that end, the inter-channel stimulated Raman scattering Gaussian noise (ISRS GN) integral model is extended to include these parameters. The integrals involved in this frequency-domain model are numerically solved in hyperbolic coordinates using a Riemann sum. The model implementation is designed to work on parallel graphics processing units (GPUs) and is optimised for fast computational time. The model is valid for Gaussian-distributed signals and is compared with the split-step Fourier method (SSFM), for transmission over standard single-mode fibre (SSMF) in the O-band (wavelengths around the zero-dispersion wavelength), showing reasonable agreement. Further, we demonstrated SNR evaluation over an 80 km SSFM single-span transmission using 589×96 GBaud channels, corresponding to almost 59 THz optical bandwidth, fully populating the O, E, S, C, L and U bands (1260–1675 nm). The SNR evaluation is completed in just 3.6 seconds using four Nvidia V100 16GB PCIe GPUs. Finally, we used this model to find the optimum launch power profile for this system achieving 747 Tbps of potential throughput over 80 km fibre and demonstrating its suitability for UWB optimisation routines.

Index Terms—Ultrawideband transmission, Raman amplification, Gaussian noise model, nonlinear interference, nonlinear distortion, optical fibre communications, inter-channel stimulated Raman scattering

I. INTRODUCTION

IN our increasingly interconnected world, the demand for faster and more reliable data transmission has driven the rapid evolution of optical communication systems. In the past decade, there has been research interest towards increasing optical link capacity by expanding the optical bandwidth beyond the conventional C-band. This has been accelerated by emerging research in optical amplification, such as Bismuth-doped fibre amplifiers (BDFA) capable of amplifying the original [1] and extended wavelength (O- and E-) bands, including distributed Raman-amplified links [2], [3]. Recent experimental ultrawideband (UWB) system demonstrations have convincingly shown the practical feasibility of transmitting multiple bands including the O-band, using 25 THz of bandwidth spanning original- to ultralong- (O- to U-) bands [4]. The advances in the expansion of the practically

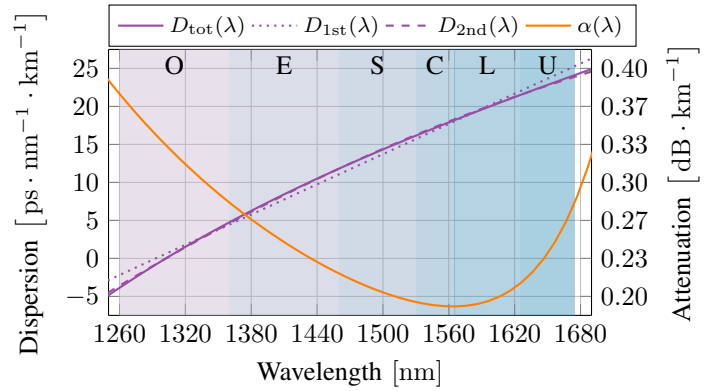


Figure 1. Modelled fibre attenuation $\alpha(\lambda)$, dispersion profile $D_{\text{tot}}(\lambda)$ and its fitting curves: $D_1(\lambda)$ considering β_2 and β_3 terms, and $D_2(\lambda)$ which also includes β_4 term.

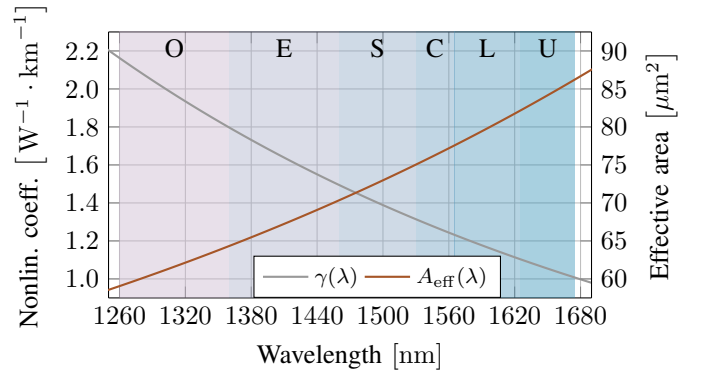


Figure 2. Modelled fibre nonlinear coefficient $\gamma(\lambda)$ and effective area $A_{\text{eff}}(\lambda)$.

feasible transmission bandwidth have, in turn, highlighted the urgent need for rapid modelling and optimisation tools.

The modelling of UWB systems enables to optimise the design of a given optical communication link to achieve maximum throughput, including finding optimal signal launch power, data rates, modulation formats, number of channels, and, in the case of hybrid-amplified links, also the Raman amplifier’s pump powers and frequencies. The Gaussian noise closed-form model (GN-CFM) expressions [5]–[9] have increasingly been used for rapid evaluation of nonlinear interference (NLI) noise, which, together with amplified spontaneous emission (ASE) noise and transceiver noise, define the received SNR. GN-CFM, in turn, can be used to optimise optical link parameters. When considering wavelength-dependent fibre parameters, the Gaussian noise (GN) model has been used to evaluate the capacity of UWB systems [10]–[12]. In most of these studies however, the O-Band is omitted or a guard-

M. Jarmolovičius, H. Buglia, M. Shevchenko, Filipe M. Ferreira, E. Sillekens, P. Bayvel and R. I. Killey are with Optical Networks Group, Department of Electronic and Electrical Engineering, UCL (University College London), London, UK

D. Semrau is with Infinera Corporation, 9005 Junction Drive, Annapolis Junction, MD 20701, USA

band is placed in the zero dispersion region [13], [14], thus, not assessing the potential capacity increase brought by the channels in this band. The guard-band is placed as GN-CFM expressions lack multichannel interference (MCI) expressions arising from four-wave mixing, causing them to underestimate NLI in the case of low chromatic dispersion. This is especially critical for channels around the zero dispersion wavelength of the fibre. The GN-CFM in [15] includes MCI expressions, making it valid for multi-channel simulations at and close to zero-dispersion wavelength; however, it does not include inter-channel stimulated Raman scattering (ISRS) terms, making it unsuitable for UWB and scenarios with distributed and hybrid amplification technologies.

In this work, we present, for the first time, an ISRS Integral GN model for UWB transmission including the O-band and channels covering the zero-dispersion wavelength. We have validated the accuracy of this model at zero-dispersion wavelength with a split-step Fourier Method (SSFM) from 1 to 101 channel transmission. Furthermore, we extended the GN model to include the higher-order dispersion terms of the wavelength-dependent parameters to increase accuracy covering over 415 nm modulated bandwidth. Finally, we have implemented a fast numerical integral GN model on multiple graphics processing units (GPUs) to demonstrate a 589×96 GBaud channels transmission launch power optimisation. This is the first model predicting the performance of a fully loaded O-to-U band transmission without guard bands at zero-dispersion wavelength, which is also capable of estimating the quality of transmission for distributed Raman and hybrid amplification.

The rest of the paper is as follows. In Section II, we estimate wavelength-dependent parameters suitable for UWB simulation by modelling standard single-mode fibre (SSMF). In Section III, we present a parallelised and GPU-accelerated implementation of the numerical GN integral model GN model NLI results are compared with the SSFM simulation, considering transmission in the O-band around the zero-dispersion wavelength. In Section IV, we used the implementation of the GN integral model to optimise the launch power in the UWB transmission system. Appendix A describes the mathematical framework for the integral GN model. Appendix B presents the higher dispersion order expressions for the GN-CFM.

II. ULTRAWIDEBAND FIBRE MODEL

This section describes the fibre model, which was used to obtain wavelength-dependent parameters suitable for UWB transmission simulations. The contribution of the higher-order dispersion, nonlinear coefficient (γ) and effective core area (A_{eff}) terms becomes non-negligible when increasing total signal optical bandwidth. We employ a mode solver exploring the azimuthal symmetry of optical fibers [16] to estimate all of these terms as it would be challenging to measure them experimentally over a very large bandwidth. The mode solver models electromagnetic surface waves along a dielectric waveguide using Maxwell's equations. Unknown propagation coefficients are obtained by numerically solving differential equations with imposed boundary conditions [17].

In our study, we consider a single-step index fibre with 8.2 μm core diameter and relative core-cladding index difference $\Delta = 0.36\%$. We assume no cladding trench or refractive index gradient. The results of the mode solver are shown in Fig. 1 and 2.

The fibre attenuation profile shown in Fig. 1 is modelled considering the Rayleigh scattering and the infrared absorption [10, Eq. (1)] to match commercially available SSMFs. The fibre is assumed to not have OH^{-1} ions absorption or other peaks.

The total dispersion D_{tot} obtained by the mode solver is shown in Fig. 1. D_{tot} is fit using first ($D_{1\text{st}}$) and second ($D_{2\text{nd}}$) order polynomials. Polynomial coefficients directly correspond to the chromatic dispersion parameter D , dispersion slope S and dispersion curvature \dot{S} . We can find second (β_2), third (β_3) and fourth (β_4) order group velocity dispersion parameters by using (1), (2) and (3), respectively:

$$\beta_2(\lambda) = -\frac{D\lambda^2}{2\pi c}, \quad (1)$$

$$S \triangleq \left(\frac{\partial D}{\partial \lambda}\right)_{\lambda=\lambda_c}, \quad \beta_3(\lambda) = \frac{\lambda^3}{(2\pi c)^2} (2D + S\lambda), \quad (2)$$

$$\dot{S} \triangleq \left(\frac{\partial S}{\partial \lambda}\right)_{\lambda=\lambda_c}, \quad \beta_4(\lambda) = -\frac{\lambda^4}{(2\pi c)^3} (6D + 6S\lambda + \dot{S}\lambda^2). \quad (3)$$

Centre wavelength is denoted as λ_c . The average error over the wavelength range of 1260–1675 nm between the D_{tot} and $D_{1\text{st}}$ is 0.58 ps · nm⁻¹ · km⁻¹ with a maximum error of 1.7 ps · nm⁻¹ · km⁻¹ at 1260 nm. Modelled D_{tot} zero-dispersion wavelength λ_{zd} is at 1302.3 nm. The $D_{1\text{st}}$ approximation has zero-dispersion at 1293 nm, which is a large 9.3 nm error. With a higher-order β_4 term, the average error between the D_{tot} and $D_{2\text{nd}}$ is 0.089 ps · nm⁻¹ · km⁻¹ with a maximum of 0.28 ps · nm⁻¹ · km⁻¹ at 1260 nm. The zero-dispersion wavelength error is insignificant, i.e., 0.05 nm.

The wavelength-dependent effective core area A_{eff} and the nonlinear coefficient γ are shown in Fig. 2. γ depends on two wavelength-dependent components – the A_{eff} and the nonlinear (Kerr) refractive index n_2 , shown in (4):

$$\gamma(\lambda) = \frac{2\pi}{\lambda} \cdot \frac{n_2(\lambda)}{A_{\text{eff}}(\lambda)}. \quad (4)$$

The nonlinear refractive index depends on two other wavelength-dependent components as shown in (5). The first one is the linear refractive index n_0 , which we acquire from the mode solver. The second one is the real component of the third-order optical susceptibility, which is a fourth-rank tensor denoted as $\chi_{xxxx}^{(3)}$. Its value is also wavelength dependent, we consider a linear fit based on two points reported in [18].

$$n_2(\lambda) = \frac{3}{4\epsilon_0 c n_0^2(\lambda)} \Re \left\{ \chi_{xxxx}^{(3)} \right\}, \quad (5)$$

where c is the speed of light in vacuum and ϵ_0 is the vacuum permittivity. Intermodal crosstalk due to coupling between the fundamental and higher-order fibre modes is assumed to be negligible.

For the following simulations, we use the measured ITU-T G652.D fibre Raman gain profile [5, Fig. 1b] and scaled at different wavelengths by the value $A_{\text{eff}}(\lambda)$.

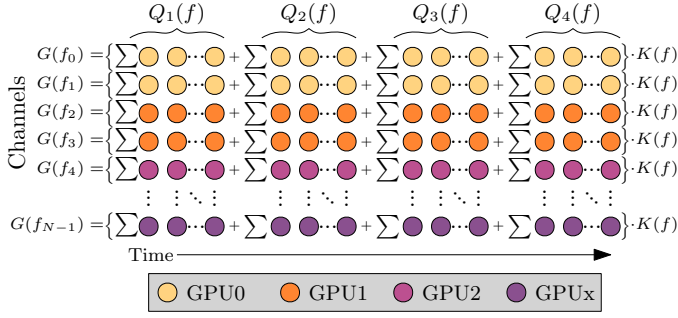


Figure 3. A diagram for the parallel computation progress. Rows represent each channel GN integral NLI solution $G(f)$ using Riemann sum. Each coloured circle represents the computation of a single Riemann sum step for a single quadrant Q_κ with N_R per samples per quadrant. K represents channel constants outside the integral.

III. INTEGRAL GN MODEL IMPLEMENTATION

In this section, we describe the numerical GN model implementation, optimal computation parameters, and its accuracy at zero-dispersion wavelength. We based it on the ISRS GN integral model introduced in [19]. The model is used for the per-channel NLI estimation and is valid for signals with Gaussian-distributed constellations. We extend the ISRS GN integral model to include frequency-dependant nonlinear coefficient (γ), and effective core area.

It is further expanded by assuming that the optical power along fibre distance is slowly varying and can be approximated by dividing it into discrete distance steps N_M as shown in (15). The new model is shown in (6), where the power spectral density (PSD) of NLI noise $G(z, f)$, L_k is the length of fibre span k , $G_{Tx}(f)$ is signal PSD which we approximate as rectangular function for the channel bandwidth, p_k is the power profile term shown in (9), which is derived by solving Raman power evolution ordinary differential equations (ODEs), including $A_{\text{eff}}(f)$. The phase mismatch factor ϕ is extended to include a higher-order β_4 dispersion in (10). We define the Fourier transform as $\mathfrak{F}\{f(x)\}(t) \triangleq \int_{-\infty}^{+\infty} f(x)e^{-j2\pi tx} dx$ and $\text{sinc}(x) \triangleq \frac{\sin(x)}{x}$. The mathematical derivations can be found in Appendix A.

$$G(z, f) \approx \frac{16}{27} \gamma^2(f) \int df_1 \int df_2 G_{Tx}(f_1) G_{Tx}(f_2) \cdot G_{Tx}(f_1 + f_2 - f) \cdot \left| \sum_{k=1}^n \sum_{\forall m} p_k(f_1, f_2, \tilde{z}_m) \cdot \Delta z_m e^{j\phi(f_1, f_2)(\tilde{L}_k + z_m)} \text{sinc}\left(\phi(f_1, f_2) \frac{\Delta z_m}{2}\right) \right|^2, \quad (6)$$

The frequency integrals are further transformed to four quadrants Q_κ in hyperbolic formulation in (20) to (23). For numerical implementation, we use Riemann sum to solve Q_κ . NLI evaluation for every channel is highly parallelisable as NLI computation is independent for each channel. Channels are organised into groups equally distributed to the available GPUs for computation of their respective NLI (each group represented in different colours in Fig. 3). Each GPU concurrently computes multiple channels with a batch, one Riemann sum term at a time (each circle in Fig. 3). Each integral quadrant

(Q_κ) is computed one after another. This approach maximises each GPU utilisation, significantly reducing computation time.

The code was implemented in Python with JAX framework [20], and all operations were performed using double-precision (64 bit) floating-point numbers.

A. Numerical model parameters

In this subsection, our objective is to investigate the accuracy of the NLI of the GN integral model and the computation time trade-offs with different values of the number of Riemann samples (N_R); and distance steps N_M along the fibre length. Steps N_M are sampled in log-scale distance intervals, with more steps at the start of the fibre where the highest optical power is. The mean number of steps per km is defined as $\bar{N}_M = (N_M - 1)/L \cdot 10^3$ where L is fibre length.

We consider the UWB transmission scenario described in Table II with the fibre parameters from Fig. 1 and Fig. 2. We use spectrally uniform launch power of 2 dBm per channel. We start NLI evaluation $\eta_{\text{NLI},0}^{\text{dB}}$ with large values of $N_R = 500$ and $\bar{N}_M = 2$ to ensure high accuracy results. Next, we sweep through NLI values $\eta_{\text{NLI},x}^{\text{dB}}$ with N_R ranging from 25 to 250 and \bar{N}_M ranging from 0.1 to 1.5 steps/km. Fig. 4a shows the computation time in seconds for NLI estimation obtained with the different values of N_R and N_M using four Nvidia V100 16GB PCIe GPUs. The difference between high accuracy NLI results and swept results $|\eta_{\text{NLI},0}^{\text{dB}} - \eta_{\text{NLI},x}^{\text{dB}}|$ are shown

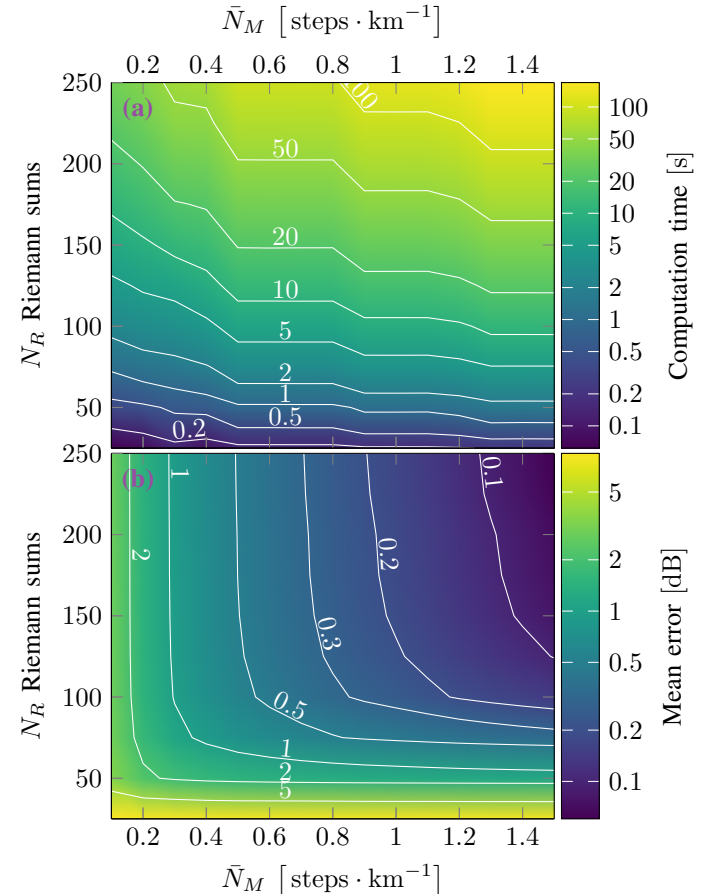


Figure 4. (a) Computation time and (b) accuracy versus numerical GN integral model parameters.

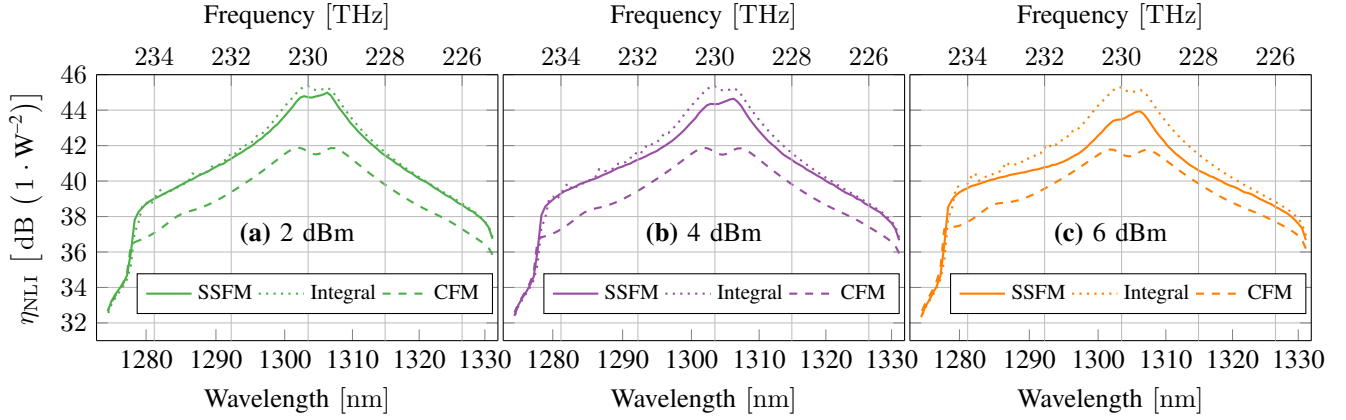


Figure 5. Nonlinear interference (η_{NLI}) solutions for 101 channel transmission centered at λ_{zd} . The figure compares SSFM, Integral, and GN CFM models. Only three cases are shown for 2 dBm, 4 dBm and 6 dBm launch power per channel. The optimum power in this scenario is 0.25 dBm per channel.

in Fig. 4b. The results show a trade-off between speed and accuracy is in favour of larger \bar{N}_M rather than large N_R values. For cases where $N_R = 75$, $\bar{N}_M = 0.95$, taking 3.6 seconds to compute resulting in 0.46 dB NLI error; $N_R = 150$, $\bar{N}_M = 1.4$ taking 37 seconds and resulting in < 0.1 dB NLI error. These parameter values can be selected depending on the desired accuracy and execution time.

B. Model accuracy at zero dispersion

The accuracy of the proposed integral GN model is validated around the zero dispersion wavelength of the fibre through comparisons with SSFM simulations. It is infeasible to simulate a transmission occupying O-to-U bands as it requires a large number of channels which makes SSFM computation expensive. Therefore, here, we limit our accuracy comparison to up to 101 channels. GN integral model has previously been validated for S, C and L bands [5], [21], therefore we simulate in the O-band, at the zero-dispersion wavelength i.e. at $\lambda_{\text{zd}} = 1302.3$ nm, where the highest error is expected due to dispersion being a dominant term in the interplay between phase mismatch factor (ϕ), γ and ISRS effects. O-band validation simulation includes the wavelength-dependent fibre parameters as described in section II, except that we considered a constant nonlinear coefficient of $\gamma(\lambda_{\text{zd}}) \simeq 2 \text{ W}^{-1} \cdot \text{km}^{-1}$ – this is because we do not include frequency-dependent γ in the SSFM algorithm. We consider the channel spacing and symbol rate shown in Table II, transmitted over 80 km single fibre span. We simulated ten scenarios with the number of channels ranging from 1 to 101, centred at the λ_{zd} . Each of these scenarios is simulated with five different launch powers: –2 dBm, 0 dBm, 2 dBm, 4 dBm and 6 dBm per channel. The SSFM simulation considers 2^{16} random Gaussian symbols per polarisation per channel with two samples per symbol and a root-raised-cosine filter with a roll-off factor of 1%. Step sizes for the SSFM simulation were optimised using the local-error method [22] using a small goal error value of $\delta_G = 10^{-10}$ to ensure accurate results. The integral model was solved using $\bar{N}_M = 1.4$ steps and $N_R = 150$, based on results found in Subsection III-A.

For the accuracy metric, we define the channel-wise error between the integral GN model and the SSFM as

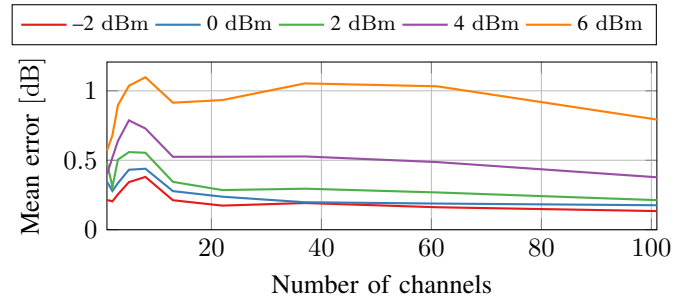


Figure 6. Comparing difference between SSFM and GN model nonlinear interference (η_{NLI}) in O-Band.

$|\eta_{\text{NLI,GN}}^{\text{dB}} - \eta_{\text{NLI,SSFM}}^{\text{dB}}|$. We evaluate this error for ten different channels and five different launch powers, with the average channel error shown in Fig. 6. The error decreases when increasing the number of channels, with a maximum of 1 dB error with three channels at 6 dBm launch power, decreasing to 0.79 dB error at 101 channels. The same trend is observed with 4 dBm, 2 dBm, 0 dBm and –2 dBm launch power scenarios.

We plot NLI per channel for the 101 channel scenario case in Fig. 5. The mean and maximum channel error, together with the total optical power are shown in Table I. The maximum NLI error is 1.8 dB in the channel with the highest NLI at 1303.4 nm being for the case with 6 dBm launch power per channel shown in Fig. 5c. This demonstrates an extreme case where launch power is much greater than optimum as discussed later in this section. The maximum NLI error is followed by 1 dB at the same wavelength for the scenario with 4 dBm per channel in Fig. 5b and 0.7 dB error at 1277.9 nm with 2 dBm per channel in Fig. 5a. For lower launch powers, the maximum NLI error per channel is below 0.6 dB. For all the cases good agreement is found between integral and SSFM models in channels that are located further away from the highest NLI point as can be seen in channels below 1292 nm and above 1315 nm in Fig. 5b and channels below 1287 nm and above 1321 nm in Fig. 5c. The error between the GN model and the SSFM is expected to be larger for high launch powers because of the first-order regular perturbation assumption underlying the derivation of the GN model, which results in a NLI overestimation.

For the same 101 channel scenario, we also include, for

Table I
 η_{NLI} ERROR BETWEEN SSFM, NUMERICAL GN INTEGRAL MODEL AND GN CLOSED-FORM MODEL IN 101 CHANNEL SCENARIO

Ch. Launch power [dBm]	-2	0	2	4	6
Tot. Launch power [dBm]	18	20	22	24	26
SSFM vs. GN-Int. Max. [dB]	0.13	0.18	0.21	0.38	0.79
SSFM vs. GN-Int. Mean [dB]	0.65	0.59	0.72	1.02	1.81
SSFM vs. GN-CFM Max. [dB]	1.84	1.78	1.75	1.58	1.14
SSFM vs. GN-CFM Mean [dB]	3.47	3.39	3.28	2.99	2.37

comparison, the results obtained using the GN-CFM [7], which were expanded to support the higher order β_4 dispersion term, as described in the Appendix B. Estimation of NLI using GN-CFM is shown in Fig. 5. The average and maximum channel error of $\eta_{\text{NLI}}^{\text{dB}}$ is shown in Table I. The large error is expected because GN-CFM lacks MCI expressions, making it underestimate NLI. The results show that the NLI error decreases with higher launch power, but this is simply because the NLI is overestimated due to the first-order regular perturbation assumption, combined with the NLI underestimation due to lack of MCI expressions.

Additionally, the optimisation algorithm of Section IV is used to find the spectrally uniform optimal launch power for the 101 channel scenario described in this section, considering uniform 7 dB amplifier noise figure. This resulted in 0.254 dBm per channel (20.3 dBm total optical power). The integral GN model shows good agreement with SSFM NLI results close to optical launch power and at higher optical powers.

IV. LAUNCH POWER OPTIMISATION

In this section, we demonstrate the practical application of the fast numerical ISRS GN model evaluation on a GPU by optimising channel launch powers to maximise total data throughput. The transmission scenario is outlined in Table II and optimisation is performed by using the L-BFGS-B algorithm [23]. This algorithm was chosen because it efficiently finds a local minimum with a large problem dimensionality, with finite-differences gradient estimation. To simplify the problem, we reduced the number of optimisation dimensions by dividing the spectral window into segments for power optimisation. The number of segments per band is defined as $N_B = \text{round}(B_{\text{band}}/B_p)$, where B_{band} is the total bandwidth

Table II
 SIMULATION PARAMETERS

# of channels (N_{ch})	589	
# of guard channels (N_A)	32	
Modulation format	Gaussian	
Symbol rate	96	GBaud
Channel spacing	100	GHz
Reference wavelength (λ_c)	1438	nm
Fibre length (L)	80	km
Dispersion (D)	17.74	$\text{ps} \cdot \text{nm}^{-1} \cdot \text{km}^{-1}$
Dispersion slope (S)	0.057	$\text{ps} \cdot \text{nm}^{-2} \cdot \text{km}^{-1}$
Dispersion curvature (\tilde{S})	$-5.975 \cdot 10^{-5}$	$\text{ps} \cdot \text{nm}^{-3} \cdot \text{km}^{-1}$
Guard band gap	5	nm

Table III
 PER BAND CHARACTERISTICS

Band	O	E	S	C	L	U
Amp. noise figure [dB]	7	7	7	5	6	8
Num. of channels	171	143	88	38	65	52
Num. of opt. segments	23	10	6	3	4	3

of each band and B_p approximate segment bandwidth, which value we chose as 75 GHz in the case of O-Band and 150 GHz for all other bands. These segments are equally spaced within the band with a minimum of two edges per band. We optimise segment edges, whose values are represented in the dBm scale, as this allows the optimiser to effectively search for positive and negative values in the logarithmic domain. The optimisation was bounded from -5 dBm to 5 dBm. Channel powers were linearly interpolated between the segments' edges, enabling the optimiser to evaluate more complex power profiles for each band. Despite that the L-BFGS-B algorithm does not guarantee finding the global minimum solution, we consider the solution to be approaching towards the optimum, considering the practical application [24].

The cost function is defined as the link throughput shown in (7), where N_{ch} is the number of channels and A denotes a subset of all channels that we leave empty, i.e., the set of guard bands. P_i is the channel power and $\eta_{\text{NLI},i}$ is NLI noise factor per channel. $P_{\text{ASE},i}$ is ASE noise variance per channel and we assume all band amplifiers ideally compensate for lost power back to optimised launch power profile.

$$\mathcal{L} = - \sum_{i=0, i \notin A}^{N_{\text{ch}}} \log_2 \left(1 + \frac{P_i}{\eta_{\text{NLI},i} \cdot P_i^3 + P_{\text{ASE},i}} \right). \quad (7)$$

A uniform 0 dBm per band launch power was used as the

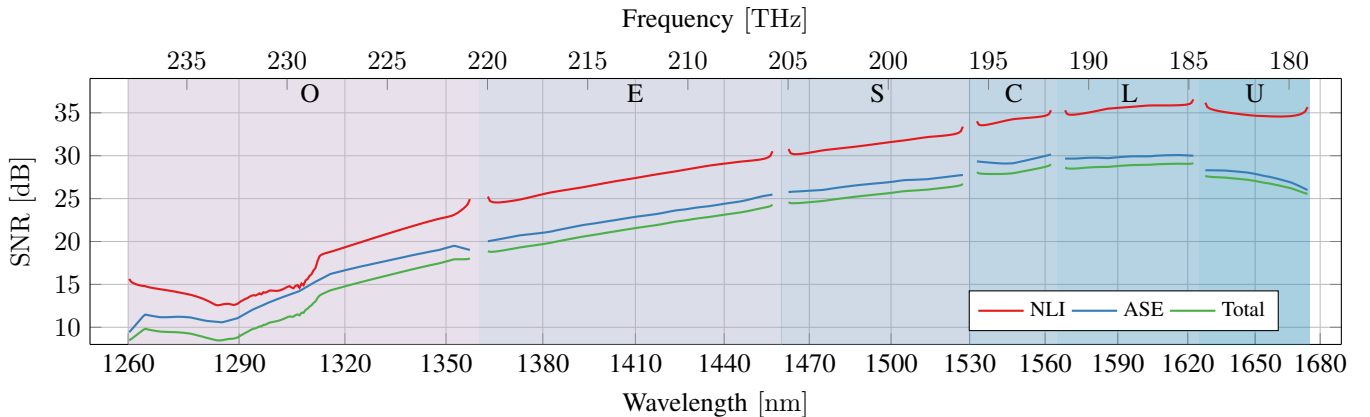


Figure 7. SNR result after launch power optimisation for single 80 km fibre span, including nonlinear interference (NLI) and ASE noise. NLI is evaluated with a numerical GN integral model, including $A_{\text{eff}}(f)$, $\gamma(f)$, $\beta_2(f)$, $\beta_3(f)$ and $\beta_4(f)$ terms.

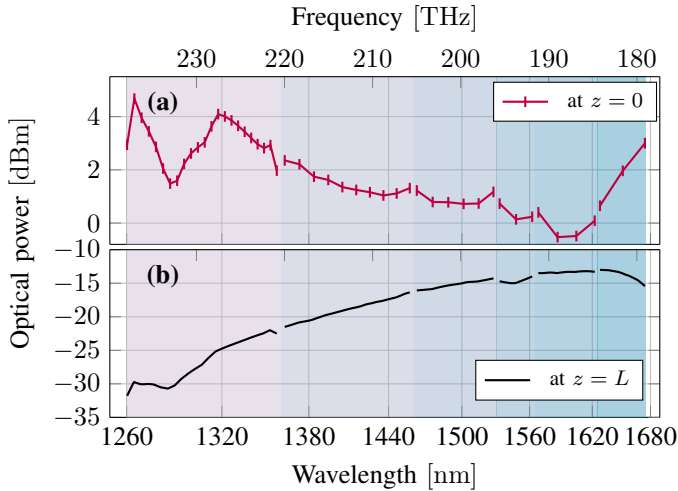


Figure 8. Transmitted optimised launch power (a), and optical power at the end of span (b), $L = 80$ km. Each vertical line represents a segment edge which is controlled by the optimiser and channel launch power is linearly interpolated between these edges.

initial condition. The optimiser is run with stop condition of $\max(|\nabla \mathcal{L}|) \leq 0.01$. The four Nvidia V100 16GB PCIe GPUs completed the optimisation task in 641 seconds using $N_R = 75$ and $\bar{N}_M = 1$. We then re-ran the optimisation with these results as the initial condition and with higher accuracy parameters of $N_R = 150$ and $\bar{N}_M = 1.4$ to fine-tune the solution. This took another 72 minutes.

The results of the launch power optimisation are shown in Fig. 8a, together with received power after ISRS effects in Fig. 8b. The total optical power launched into the fibre using optimised parameters is 29.4 dBm, and per-band powers are shown in Table IV. All bands show a simple launch power profile, indicating that the optimisation using the segment scheme is a good approximation, compared to a more expensive per-channel optimisation scheme. O-Band has a more complex profile and this is the reason for using a smaller B_p segment bandwidth. The peak launch power of 4.7 dBm was observed at 1264.5 nm, where fibre loss is highest. The lowest launch power optimisation segment edge of 1.54 dBm is at 1285.7 nm, which indicates the highest NLI region. Comparing this highest NLI region to the model accuracy at zero dispersion results in Subsection III-B we can conclude that the model should be accurate for this power optimisation scenario for the given low launch power in this region.

The SNR results together with NLI and ASE noise are shown in Fig. 7. The O-Band exhibits the worst performance and noise variation, with the lowest and highest SNR of 8.3 dB and 17.8 dB respectively. C, L and U bands show the lowest

channel noise with a mean SNR of 27.7 dB, 28.4 dB and 26.6 dB respectively.

We estimated the potential link throughput at the Shannon rate $C = -2B_{ch} \cdot \mathcal{L}$ with B_{ch} being the channel bandwidth; resulting in 747 Tbps when optimised using power segment method. The capacity per band is shown in Table IV Case 1. We use the same optimisation algorithm to find optimal launch power with all channels having uniform power across all bands resulting in 1.87 dBm per channel (29.33 dBm total power) and 739 Tbps of potential throughput, per band capacity is shown in Table IV Case 2.

V. CONCLUSION

In this work, we model the ultrawideband optical transmission, covering 1260 nm to 1675 nm, taking into account wavelength-dependent fibre parameters, including dispersion curvature, nonlinear coefficient and effective fibre core area. We have extended the GN integral model to include these parameters and described its solution using the slowly varying power approximation along the fibre length and frequency integral in hyperbolic coordinates. The GN integral was numerically solved using a Riemann sum, and implementation was optimised for fast and efficient parallel GPU computing. Algorithm parameters were investigated, to achieve a good trade-off between accuracy and computation time. This model includes multi-channel interference (four-wave mixing), enabling accurate simulations for O-band transmission around the λ_{zd} (zero-dispersion wavelength). This was confirmed through comparisons with SSFM-based modelling, showing good agreement across the O-band centred at λ_{zd} , with an average error in the NLI of only 0.21 dB with 101 channels at 2 dBm launch power per channel, while a solution obtained using the GN closed-form expressions resulted in mean channel error of 1.75 dB NLI. The average error of the numerical integral NLI solution decreases with a larger number of channels and lower launch powers.

The SNR calculation takes just 3.6 seconds for O-to-U band transmission over 80 km using four Nvidia V100 16GB PCIe GPUs. We have optimised launch power in a fully loaded O-to-U band system, using the L-BFGS-B algorithm. For a link length of 80 km, the optimisation task with our implementation was completed under 83 minutes, using the same four GPUs.

This model can be used to investigate several other parameters, such as channel symbol rate and spacing, distributed Raman amplification pump powers and wavelengths. Future work will include the investigation of numerical accuracy with multiple spans and constellation correction terms. In addition, a more advanced lumped amplifier gain model should be considered to achieve a closer representation of realistic system scenarios.

ACKNOWLEDGMENTS

This work is partly funded by the EPSRC Programme Grant TRANSNET (EP/R035342/1), EWOC (EP/W015714/1), and UKRI Future Leaders Fellowship (MR/T041218/1). M. Jarmolovičius and H. Buglia are funded by the Microsoft 'Optics for the Cloud' Alliance and a UCL Faculty of Engineering Sciences Studentship.

Table IV

PER BAND CHARACTERISTICS IN OPTIMISED POWER SEGMENT SCENARIO (CASE 1) AND SPECTRALLY UNIFORM OPTICAL LAUNCH POWER (CASE 2). "POW." REPRESENTS TOTAL OPTICAL POWER PER BAND, AND "CAP." REPRESENTS POTENTIAL THROUGHPUT.

Band	O	E	S	C	L	U
Case 1 pow. [dBm]	25.6	23.2	20.5	16.3	18.0	19.4
Case 2 pow. [dBm]	24.2	23.4	21.3	17.7	20.0	19.0
Case 1 cap. [Tbps]	139.6	193.2	141.0	67.1	117.7	88.4
Case 2 cap. [Tbps]	139.8	189.0	134.6	66.4	119.3	89.8

DATA AVAILABILITY STATEMENT

The data that support the figures in this paper are available from the UCL Research Data Repository (DOI: 10.5522/04/24975612), hosted by FigShare.

 APPENDIX A
 NUMERICAL GAUSSIAN NOISE MODEL

In this section, we describe in detail the mathematical derivation of Gaussian Noise Model improvements to support wavelength dependent parameters, approximating power as slowly varying along fibre length integral, and interal in hyperbolic coordinates.

We start with the integral expression [19, Eq. (4)] in (8). We include the sum operation for multi-span systems, with n number of spans. In the case of identical spans, this summation is reduced to the phased-array term shown in [19, Eq. (5)]. $\rho(z, f)$ is the normalised power profile obtained by numerically solving the Raman power evolution profile [5, Eq. (1)] using ODEs, where Raman gain spectrum $g_r(\Delta f)$ is scaled by the effective area at the channel frequency f_i .

$$G(z, f) = \frac{16}{27} \gamma^2(f) \int df_1 \int df_2 \quad (8)$$

$$\cdot G_{\text{Tx}}(f_1) G_{\text{Tx}}(f_2) G_{\text{Tx}}(f_1 + f_2 - f) \cdot \left| \sum_{k=1}^n \int_0^{L_k} d\zeta \right. \\ \left. \cdot \sqrt{\frac{\rho(\zeta, f_1) \rho(\zeta, f_2) \rho(\zeta, f_1 + f_2 - f)}{\rho(\zeta, f)}} e^{j\phi(f_1, f_2, f, L_k + \zeta)} \right|^2.$$

We simplify normalised power profile terms as follows:

$$p_k(f_1, f_2, \zeta) = \sqrt{\frac{\rho(\zeta, f_1) \rho(\zeta, f_2) \rho(\zeta, f_1 + f_2 - f)}{\rho(\zeta, f)}}. \quad (9)$$

We approximate the non-linear coefficient γ to be constant within the channel bandwidth. Furthermore, we assume that all interfering channels have the same γ as the channel itself, as the most NLI contribution for the channel is local and further spaced channels with the largest γ error will have the lowest contribution. This assumption allows us to simply keep the $\gamma(f)$ term outside the integral as shown in (8).

The phase mismatch factor ϕ is derived by extending dispersion Taylor series to include the fourth-order dispersion coefficient β_4 in [19, Eq. (13)] and factoring $\phi(f_m, f_k, f_0, \zeta) = [\Gamma(\zeta, f_m) + \Gamma^*(\zeta, f_m + f_k - f_0) + \Gamma(\zeta, f_k) - \Gamma(\zeta, f_0)]/j$. This results in (10), similar to [11, Eq. (3)]:

$$\phi(f_1 + f, f_2 + f, f, \zeta) = -4\pi^2 f_1 f_2 \left[\beta_2 + \pi \beta_3 (f_1 + f_2 + 2f) \right. \\ \left. + \frac{2\pi^2 \beta_4}{3} [f_1^2 + \frac{3}{2} f_1 f_2 + 3f_1 f_i + f_2^2 + 3f_2 f_i + 3f_i^2] \right] \zeta. \quad (10)$$

We assume power $p_k(f_1, f_2, \zeta)$ is slowly varying, therefore it can be approximated with a sum of discrete distance steps m along the fibre length. m values are distributed in logarithmically increasing distance steps to have approximately equal power change per step. This is shown in (12) to (15), where Δz_m is the step size distribution with z_m midpoints. \tilde{z}_m is the distance at which the power profile is evaluated within each

step. In Subsection III-A we demonstrate that error is small given the large enough number N_M of m steps.

$$\sum_{k=1}^n \int_0^{L_k} p_k(f_1, f_2, \zeta) \cdot e^{j\phi(f_1, f_2, \tilde{L}_k + \zeta)} d\zeta \quad (11)$$

$$\approx \sum_{k=1}^n \sum_{\forall m} p_k(f_1, f_2, \tilde{z}_m) \int_{z_1(m)}^{z_2(m)} e^{j\phi(f_1, f_2, \tilde{L}_k + \zeta)} d\zeta \quad (12)$$

$$= \sum_{k=1}^n \sum_{\forall m} p_k(f_1, f_2, \tilde{z}_m) \cdot \frac{e^{j\phi[f_1, f_2, \tilde{L}_k + z_2(m)]} - e^{j\phi[f_1, f_2, \tilde{L}_k + z_1(m)]}}{j\phi(f_1, f_2)} \quad (13)$$

$$= \sum_{k=1}^n \sum_{\forall m} p_k(f_1, f_2, \tilde{z}_m) \cdot e^{j\phi(f_1, f_2, \tilde{L}_k + z_m)} \cdot \frac{e^{j\phi(f_1, f_2) \Delta z_m / 2} - e^{-j\phi(f_1, f_2) \Delta z_m / 2}}{j\phi(f_1, f_2)} \quad (14)$$

$$= \sum_{k=1}^n \sum_{\forall m} p_k(f_1, f_2, \tilde{z}_m) \cdot e^{j\phi(f_1, f_2) (\tilde{L}_k + z_m)} \cdot \Delta z_m \text{sinc}\left(\phi(f_1, f_2) \frac{\Delta z_m}{2}\right). \quad (15)$$

This approximation in (15) is applied to (8) yielding our integral model in (6). The frequency integral is solved for the entire signal bandwidth $\int_{-B}^{+B} df_1 \int_{-B}^{+B} df_2 \Psi(f_1, f_2)$ where $\Psi(f_1, f_2)$ is a generic function and B is half of the total bandwidth. The function is recentered at the channel frequency f , and split into four quadrants Q_κ , where $\kappa = \{1, 2, 3, 4\}$. Integration limits are swapped, resulting in quadrants with limits between $B \pm f$ and 0 as shown in (16) to (19):

$$Q_1 = \int_0^{B-f} df_1 \int_0^{B-f} df_2 \Psi(+f_1, +f_2), \quad (16)$$

$$Q_2 = \int_0^{B+f} df_1 \int_0^{B-f} df_2 \Psi(-f_1, +f_2), \quad (17)$$

$$Q_3 = \int_0^{B+f} df_1 \int_0^{B+f} df_2 \Psi(-f_1, -f_2), \quad (18)$$

$$Q_4 = \int_0^{B-f} df_1 \int_0^{B+f} df_2 \Psi(+f_1, -f_2). \quad (19)$$

Each quadrant is transformed into hyperbolic coordinates similar to [25, Section VIII]; by using $v_1 = f_1 f_2$ and $v_2 = \ln \sqrt{f_1 / f_2}$, yielding (20) to (23):

$$Q_1 = \int_0^{(B-f)^2} dv_1 \int_{-\ln\left(\frac{B-f}{\sqrt{v_1}}\right)}^{+\ln\left(\frac{B-f}{\sqrt{v_1}}\right)} dv_2 \Psi(+g_1, +g_2), \quad (20)$$

$$Q_2 = \int_0^{(B+f)(B-f)} dv_1 \int_{-\ln\left(\frac{B-f}{\sqrt{v_1}}\right)}^{+\ln\left(\frac{B+f}{\sqrt{v_1}}\right)} dv_2 \Psi(-g_1, +g_2), \quad (21)$$

$$Q_3 = \int_0^{(B+f)^2} dv_1 \int_{-\ln\left(\frac{B+f}{\sqrt{v_1}}\right)}^{+\ln\left(\frac{B+f}{\sqrt{v_1}}\right)} dv_2 \Psi(-g_1, -g_2), \quad (22)$$

$$Q_4 = \int_0^{(B-f)(B+f)} dv_1 \int_{-\ln\left(\frac{B+f}{\sqrt{v_1}}\right)}^{+\ln\left(\frac{B-f}{\sqrt{v_1}}\right)} dv_2 \Psi(+g_1, -g_2), \quad (23)$$

where $g_1 = \sqrt{v_1}e^{v_2}$ and $g_2 = \sqrt{v_1}e^{-v_2}$. Combining quadrants with integration with hyperbolic coordinates and slowing varying power approximation, we obtain the final expression in (24) and (25):

$$G(z, f) = \frac{16}{27}\gamma^2(f) \sum_{\forall \kappa} Q_{\kappa}(f), \quad (24)$$

$$\begin{aligned} \Psi(f_1, f_2) &= G_{Tx}(f_1) G_{Tx}(f_2) G_{Tx}(f_1 + f_2 - f) \\ &\cdot \sum_{k=1}^n \sum_{\forall m} p_k(f_1, f_2, \tilde{z}_m) \cdot e^{j\phi(f_1, f_2)(\tilde{L}_k + z_m)} \\ &\cdot \Delta z_m \operatorname{sinc}\left(\phi(f_1, f_2) \frac{\Delta z_m}{2}\right). \end{aligned} \quad (25)$$

APPENDIX B

CLOSED-FORM GAUSSIAN NOISE MODEL

To include higher order dispersion terms in closed-form expression, we have to extend cross-phase modulation (XPM) contribution phase mismatch term $\phi_{i,k}$ [5, Eq. (34)] and self-phase modulation (SPM) contribution phase mismatch term ϕ_i [5, Eq. (42)] in (26) and (27), respectively. In both cases, we assume that the dispersion slope β_3 and the dispersion curve β_4 are constant over the channel bandwidth.

$$\begin{aligned} \phi(f_1 + f_i, f_2 + f_k, f_i) &= -4\pi^2 f_1 \Delta f \left[\beta_2 \right. \\ &\quad \left. + \pi\beta_3(f_1 + f_2 + f_i + f_k) + \frac{\pi^2\beta_4}{3}(2f_1^2 + 3f_1f_2 + 3f_1f_i \right. \\ &\quad \left. + 3f_1f_k + 2f_2^2 + 2f_2f_i + 4f_2f_k + 2f_i^2 + 2f_if_k + 2f_k^2) \right] \\ &\approx -4\pi^2 \left[\beta_2 + \pi\beta_3(f_i + f_k) + \frac{2\pi^2\beta_4}{3}(f_i^2 + f_if_k + f_k^2) \right] \\ &\quad \cdot (f_k - f_i)f_1 \\ &\triangleq \phi_{i,k} \cdot f_1. \end{aligned} \quad (26)$$

SPM phase mismatch has the same derivation as (10).

$$\begin{aligned} \phi(f_1 + f_i, f_2 + f_i, f_i) &\approx -4\pi^2 f_1 f_2 \left[\beta_2 + 2\pi\beta_3 f_i + 2\pi^2\beta_4 f_i^2 \right] \\ &\triangleq \phi_i \cdot f_1 f_2. \end{aligned} \quad (27)$$

REFERENCES

- [1] D. J. Elson, Y. Wakayama, V. Mikhailov, J. Luo, N. Yoshikane, D. Inniss, and T. Tsuritani, "9.6-THz Single Fibre Amplifier O-band Coherent DWDM Transmission," *Journal of Lightwave Technology*, pp. 1–6, 2024.
- [2] A. Donodin, E. London, B. Correia, E. Virgillito, M. Tan, P. Hazarika, I. Phillips, P. Harper, S. K. Turitsyn, V. Curri, and W. Forsysiak, "Multi-band escl transmission supported by bismuth-doped and raman fiber amplification," *Journal of Lightwave Technology*, pp. 1–12, 2023.
- [3] P. Hazarika, H. Buglia, M. Jarmolovičius, E. Sillekens, M. Tan, A. Donodin, I. Phillips, P. Harper, R. I. Killey, P. Bayvel, and W. Forsysiak, "Multi-band transmission over e-, s-, c- and l-band with a hybrid raman amplifier," *Journal of Lightwave Technology*, pp. 1–10, 2023.
- [4] D. Soma, T. Kato, S. Beppu, D. Elson, H. Muranaka, H. Irie, S. Okada, Y. Tanaka, Y. Wakayama, N. Yoshikane, T. Hoshida, and T. Tsuritani, "25-THz O+S+C+L+U-band digital coherent DWDM transmission using a deployed fibre-optic cable," *ECOC*, 2023.
- [5] H. Buglia, M. Jarmolovičius, L. Galdino, R. Killey, and P. Bayvel, "A Closed-Form expression for the Gaussian noise model in the presence of Raman amplification," *Journal of Lightwave Technology*, pp. 1–13, 2023.
- [6] A. Carena, G. Bosco, V. Curri, Y. Jiang, P. Poggiolini, and F. Forghieri, "EGN model of non-linear fiber propagation," *Optics Express*, vol. 22, p. 16335, June 2014.
- [7] D. Semrau, R. I. Killey, and P. Bayvel, "A Closed-Form Approximation of the Gaussian Noise Model in the Presence of Inter-Channel Stimulated Raman Scattering," *Journal of Lightwave Technology*, vol. 37, pp. 1924–1936, May 2019.
- [8] D. Semrau, L. Galdino, E. Sillekens, D. Lavery, R. I. Killey, and P. Bayvel, "Modulation Format Dependent, Closed-Form Formula for Estimating Nonlinear Interference in S+C+L Band Systems," June 2020. arXiv:2006.04983 [eess].
- [9] A. Ferrari, M. Filer, K. Balasubramanian, Y. Yin, E. Le Rouzic, J. Kundrát, G. Grammel, G. Galimberti, and V. Curri, "GNPy: an open source application for physical layer aware open optical networks," *Journal of Optical Communications and Networking*, vol. 12, p. C31, June 2020.
- [10] N. A. Shevchenko, S. Nallaperuma, and S. J. Savory, "Maximizing the information throughput of ultra-wideband fiber-optic communication systems," *Optics Express*, vol. 30, p. 19320, May 2022.
- [11] P. Poggiolini and M. Ranjbar-Zefreh, "Closed Form Expressions of the Nonlinear Interference for UWB Systems," 2022.
- [12] A. D'Amico, B. Correia, E. London, E. Virgillito, G. Borracchini, A. Napoli, and V. Curri, "Scalable and Disaggregated GGN Approximation Applied to a C+L+S Optical Network," *Journal of Lightwave Technology*, vol. 40, pp. 3499–3511, June 2022.
- [13] A. Ferrari, A. Napoli, J. K. Fischer, N. Costa, A. D'Amico, J. Pedro, W. Forsysiak, E. Pincemin, A. Lord, A. Stavdas, J. P. F-P. Gimenez, G. Roelkens, N. Calabretta, S. Abrate, B. Sommerkorn-Krombolz, and V. Curri, "Assessment on the Achievable Throughput of Multi-Band ITU-T G.652.D Fiber Transmission Systems," *Journal of Lightwave Technology*, vol. 38, pp. 4279–4291, Aug. 2020.
- [14] T. Hoshida, V. Curri, L. Galdino, D. T. Neilson, W. Forsysiak, J. K. Fischer, T. Kato, and P. Poggiolini, "Ultrawideband Systems and Networks: Beyond C + L-Band," *Proceedings of the IEEE*, vol. 110, pp. 1725–1741, Nov. 2022.
- [15] M. R. Zefreh, F. Forghieri, S. Piciaccia, and P. Poggiolini, "Accurate closed-form model for nonlinear fiber propagation supporting both high and near-zero dispersion regimes," *Optics Express*, vol. 29, p. 10825, Mar. 2021.
- [16] F. M. Ferreira, X. Mu, F. A. Barbosa, and M. Jarmolovičius, "Mode solver for arbitrary fibre profiles azimuthally symmetric," Oct. 2022, DOI: 10.5281/ZENODO.7186485.
- [17] J. G. Dil and H. Blok, "Propagation of electromagnetic surface waves in a radially inhomogeneous optical waveguide,"
- [18] U. Gubler and C. Bosshard, "Optical third-harmonic generation of fused silica in gas atmosphere: Absolute value of the third-order nonlinear optical susceptibility $\chi^{(3)}$," *Phys. Rev. B*, vol. 61, pp. 10702–10710, Apr 2000.
- [19] D. Semrau, R. I. Killey, and P. Bayvel, "The Gaussian Noise Model in the Presence of Inter-Channel Stimulated Raman Scattering," *Journal of Lightwave Technology*, vol. 36, pp. 3046–3055, July 2018.
- [20] S. S. Schoenholz and E. D. Cubuk, "JAX, M.D. A framework for differentiable physics*," *Journal of Statistical Mechanics: Theory and Experiment*, vol. 2021, p. 124016, Dec. 2021.
- [21] D. Semrau, E. Sillekens, R. I. Killey, and P. Bayvel, "The ISRS GN Model, an Efficient Tool in Modeling Ultra-Wideband Transmission in Point-to-Point and Network Scenarios," in *2018 European Conference on Optical Communication (ECOC)*, pp. 1–3, Sept. 2018. arXiv:1808.00533 [eess].
- [22] O. Sinkin, R. Holzlohner, J. Zweck, and C. Menyuk, "Optimization of the split-step Fourier method in modeling optical-fiber communications systems," *Journal of Lightwave Technology*, vol. 21, pp. 61–68, Jan. 2003. Conference Name: Journal of Lightwave Technology.
- [23] P. Virtanen, R. Gommers, T. E. Oliphant, M. Haberland, and et al, "SciPy 1.0: Fundamental Algorithms for Scientific Computing in Python," *Nature Methods*, vol. 17, pp. 261–272, 2020.
- [24] A. Vasylychenkova, H. Buglia, E. Sillekens, R. Killey, and P. Bayvel, "Launch power optimisation for ultrawideband transmission: Achievable throughput improvement under practical constraints," 2023.
- [25] P. Poggiolini, "The GN Model of Non-Linear Propagation in Uncompensated Coherent Optical Systems," *Journal of Lightwave Technology*, vol. 30, pp. 3857–3879, Dec. 2012.